Behavior of Argon Bubbles during Continuous Casting of Steel

Brian G. Thomas, Alex Dennisov, and Hua Bai

Department of Mechanical and Industrial Engineering
University of Illinois at Urbana-Champaign
1206 West Green Street, Urbana, IL 61801.
217-333-6919

ABSTRACT

Water model experiments, mathematical models, and plant data are analyzed to understand the behavior of argon bubbles during continuous casting of steel. High-speed video pictures reveal how argon acts to protect the nozzle wall from alumina inclusions and clogging. Mathematical models reveal the importance of inclusion attachment to moving argon bubbles, as a means of inclusion removal into the mold slag. Bubble motion in the solidifying strand of a curved slab caster is simulated with a 3-D turbulent flow model. The predictions are evaluated using the results of studies on operating casters. Insights are gained into the causes of "pencil-pipe" and blister defects on the surface of the final product.

1. INTRODUCTION

Argon gas is added to the nozzle during continuous casting to deter clogging with solid inclusions. It also affects the flow pattern in the nozzle, and subsequently in the mold. In practice, argon gas is injected through the porous material or pierced holes in the nozzle wall for a slide gate system, or through the stopper-rod tip for stopper-rod system. Figure 1 shows a schematic of continuous casting tundish, nozzle, mold and four possible argon injection locations into a slide-gate nozzle. Analysis of defects in the final product, such as "pencil pipe" blister defects reveals the presence of argon bubbles, often combined with clusters of alumina inclusions. This investigation was undertaken to explore the formation of argon bubbles, using a finite-difference model to simulate their motion in the nozzle and in the mold, to understand how bubbles can attach with small inclusions and become entrapped in the solidifying shell, and finally, to investigate how to avoid defects, such as pencil pipe.

2. MEASUREMENT OF GAS INJECTION WITH A WATER MODEL

Argon bubble motion and its effect on flow depends greatly on the size of the bubbles. This is determined during the initial stages of gas injection. A significant amount of previous work [1-6] has dealt with fundamental aspects of gas injection into liquids, which is important to many different metallurgical processes. Most of this work has focused on gas injection into stagnant liquid, such as found in ladles. However, in continuous casting nozzles, argon is injected into highly turbulent molten steel, which flows transversely across the point of injection. Little work is reported on the behavior of the injected gas in such systems.

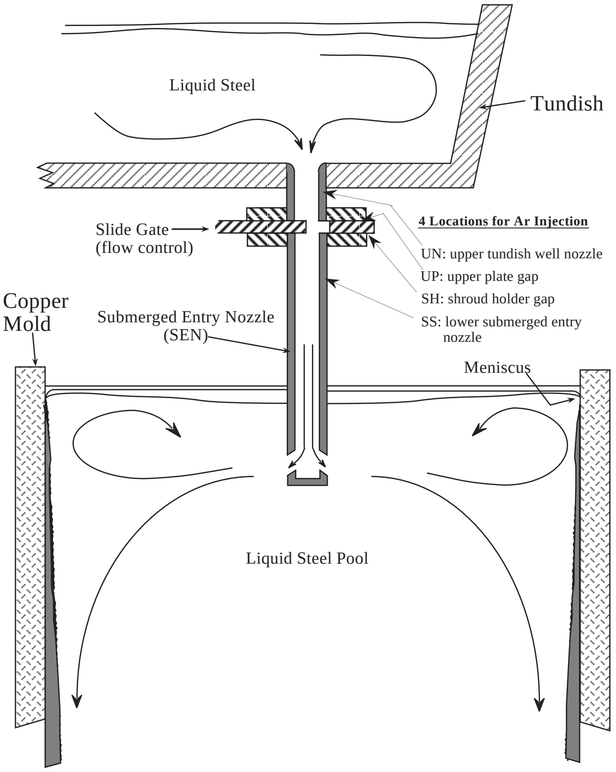

Figure 1 Schematic of the continuous casting process showing tundish, nozzle, mold and four possible argon injection locations (UN, UP, SH, and SS)

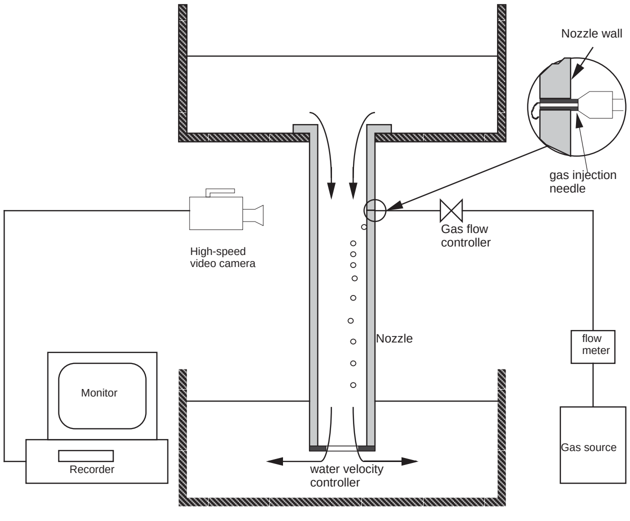

Figure 2 Schematic of the experimental apparatus

2.1 Experimental Apparatus

Figure 2 shows a schematic of the experimental apparatus. Pressurized gas (air, He, or Ar) was injected through a horizontal needle into a square 35mm X 35mm Plexiglas tube with vertical flowing water for conditions approximating those in a continuous casting nozzle. The needle outlet was flush with the nozzle wall to simulate a pierced hole or pore in a ceramic nozzle. Pressure was adjusted to achieve gas flow rates from 0.2 - 5 ml/s. The water velocity was varied from 0.9-2.5 m/s by changing the size of the opening at the bottom of the nozzle. Three different-sized needles were used to examine the effect of the gas injection “pore” diameter, (0.3, 0.4, and 0.5 mm). The formation of bubbles was recorded by a high-speed video camera at 4500 frames per second. The behavior of bubbles exiting the injection needle was studied by inspecting the video images frame by frame. Bubble diameters were measured directly from individual video image and checked by counting the number of bubbles generated at the exit of the injection needle, knowing the gas flow rate.

2.2 Bubble Size in Stagnant Liquid

Experiments were first performed with stagnant water where previous measurements and empirical correlations were available for comparison. Figure 3 shows that bubble sizes increase with increasing gas injection rate. For the same gas injection rate, a bigger pore diameter tends to produce larger bubbles. Figure 3 also shows the bubble size predicted with Iguchi’s [2] empirical correlation. The agreement between the experiment data and Iguchi’s prediction is quite reasonable. This suggests that Iguchi’s empirical correlation, which is based on relatively larger gas injection flow rates, also applies to the relatively lower gas flow rates of this work. At high gas injection rate larger bubbles emerge from larger diameter pores. However, pore size becomes less important at small gas injection rate.

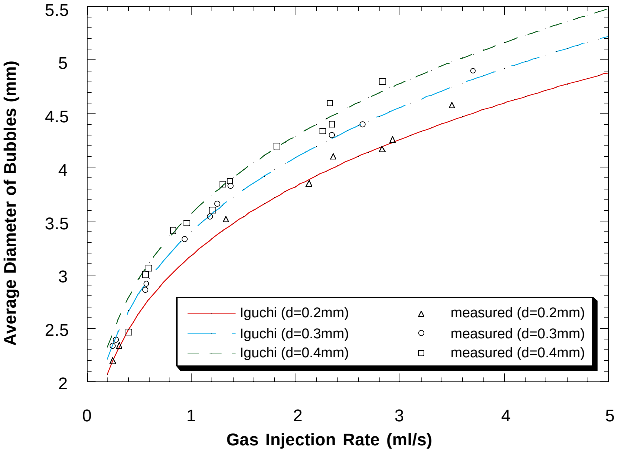

Figure 3 Measured bubble diameters in stagnant water compared with Iguchi’s empirical correlation [2]

When the gas injection flow rate is very small, the momentum of the injected gas becomes negligible. Then, a bubble begins to detach from the injection pore when the force of its buoyancy statically balances the force of surface tension holding back the bubble edges. This condition is widely reported to control the bubble size [2,7]. Unfortunately, it has little practical application in steelmaking processes where the gas injection rate is much larger.

As the gas injection rate increases, the inertia force of the injected gas begins to play an important role in bubble formation. Under this condition, the bubble formation seems to be controlled by a hydrodynamic instability, although the exact mechanism is still unclear [2].

2.3 Injection Modes in Flowing Liquid

Experiments were next performed with gas injection into flowing water. The water velocity was obtained by measuring the average velocity of tracer particles which were purposely added to the water. The transverse flow of the water across the injection exit sheared off the flow of gas and radically changed the nature of bubble formation.

It is observed that the initial shape of the bubbles exiting the gas injection pore falls into one of four distinct modes (Figure 4). For low velocity water flows (including stagnant) and small gas injection rates, Mode I is observed. In this mode, uniform-sized spherical bubbles form at the pore, then discretely detach from the wall and join the liquid stream. Mode IV is observed for high velocity water flows and large injection rates, in which each bubble elongates down along the wall, forming a sheet of gas. The sheet eventually breaks up into different size bubbles, ranging from some that are very large to others that are an order of magnitude smaller. Mode II is a transitional mode between Modes I and IV in which the injected gas generally detaches the wall but stays very near the wall. Bubbles usually elongate near the exit, but their sizes are still relatively uniform compared to those in Modes III and IV. Mode III is similar to Mode IV except there is insufficient gas flow relative to the high liquid flow to maintain a continuous gas sheet, so gaps form.

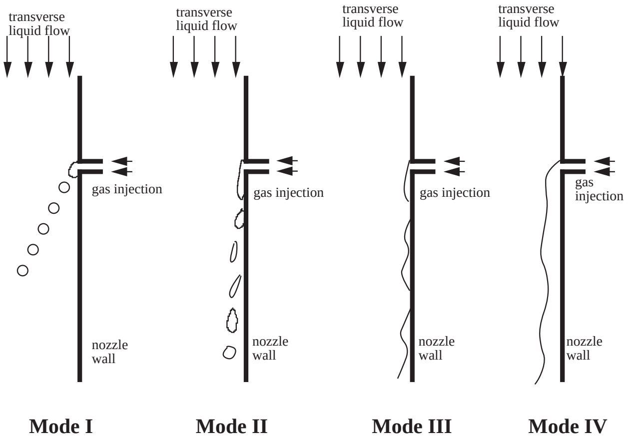

Figure 4 The four modes of injected gas behavior

It can be seen that the injected gas behavior is governed mainly by the gas injection momentum and the transverse liquid momentum. This is shown in Figure 5 where the four modes are clearly related to the Reynolds numbers for gas injection flow and transverse water flow. These Reynolds numbers are defined by:

$$\mathrm{Re}_{gas} = \frac{4Q\rho_{gas}}{\pi d\mu_{gas}} \qquad \text{and}$$

$$\mathrm{Re}_{liq} = \frac{\rho_{liq}UD}{\mu_{liq}} \qquad (1)$$

where ρ_{gas} is the gas density, ρ_{liq} is the liquid density; μ_{gas} is the gas viscosity, μ_{liq} is the liquid viscosity; d is the diameter of the gas injection pore, D is the measured bubble diameter; Q is the gas injection rate, and U is the average liquid velocity. For example, for 2mm bubbles injected at 1ml/s into 0.9 m/s liquid, Re_{gas} = 242, Re_{liq} = 2000, and the ratio Re_{gas} / Re_{liq} = 0.121. This example falls into Mode I.

The effect of surface tension is not clear at present, but does not appear to be as important as the flow rates encountered for the small surface tension in the water-gas systems.

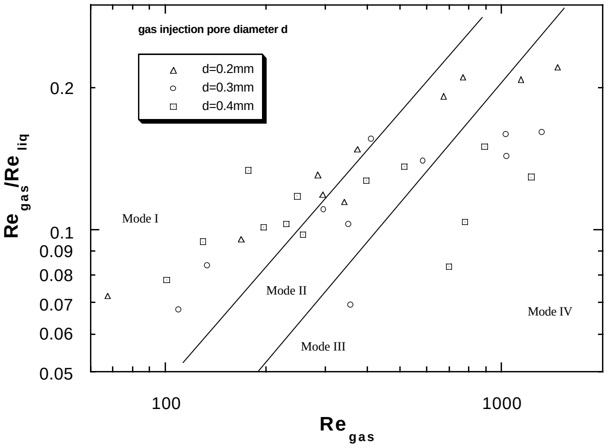

Figure 5 Gas injection modes and their relation to Reynolds numbers of the gas and liquid

2.4 Bubble Size in Flowing Liquid

The measured bubble diameter varies from 1 - 5 mm, depending on the transverse water velocity and the gas injection rate. Figure 6 shows the measured bubble diameters at different gas injection rates and the transverse water velocity for the case of 0.4mm injection pore diameter. The bubble size increases significantly with increasing gas flow rate and decreasing water velocity. Figure 7 shows the measured results at the same water velocity for three gas injection pore sizes. It appears that bubble size is independent of injection pore size. This observation is different from the observation in the case of gas injection into stagnant liquid, where bubble size increases slightly with increasing pore diameter for large gas flow rates [2].

Comparing Figures 6 and 3, it can be seen that at the same gas injection rate, the bubble size in the transverse flowing system is much smaller than in stagnant liquid. This is natural because the inertial force due to the transverse flow will shear the bubble away into the liquid stream before it grows to its maximum size, governed by hydrodynamics. The higher the velocity of the transverse flow, the smaller the formed bubble.

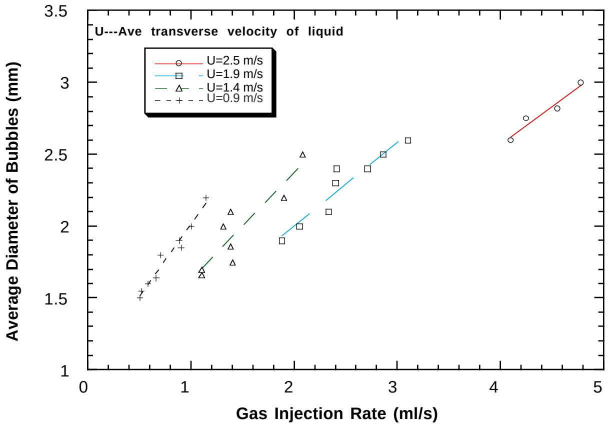

Figure 6 Measured air bubble sizes in transverse flowing water (injection pore diameter d = 0.4 mm)

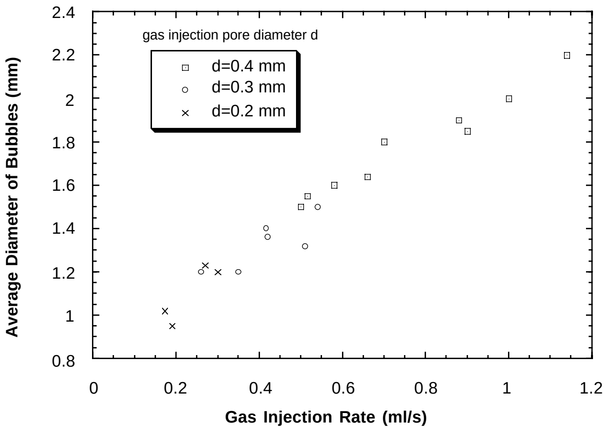

Figure 7 Effect of gas injection pore size on bubble sizes (transverse velocity of liquid U= 0.9 m/s)

Figures 6 and 7 show data collected with generally increasing gas flow with increasing water velocity. This choice of conditions was an unplanned consequence of the greater water flow inducing lower pressure at the pore, with consequently higher gas flow. The gas flow is regulated by the back pressure on the system relative to this flow-induced pressure at the pore outlet.

3. ARGON BUBBLE BEHAVIOR IN THE NOZZLE

A finite difference model has been created with the Eulerian multiphase model in FLUENT, to investigate the two-phase flow of molten steel and argon gas inside the slide gate nozzle.

In the simulations, argon gas is injected mathematically into the lower portion of the upper tundish nozzle (UN) through 14 pierced "holes" (height d=0.4mm) with a slide gate opening of 50%. The liquid steel speed was 1 m/s through a 76 mm wide nozzle. Figure 8 shows the 2-D flow pattern calculated (a) without argon injection, (b) with 10% volume fraction (hot) of 3-mm diameter argon bubbles, and (c) the corresponding gas volume fraction.

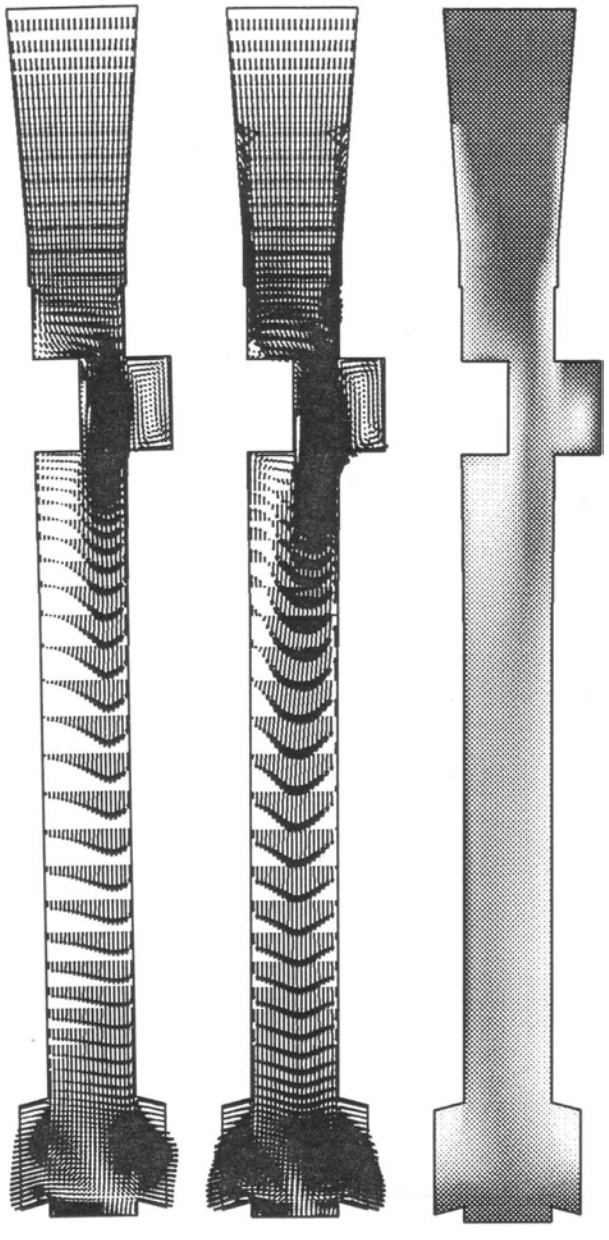

(a) (b) (c)

Figure 8 Flow Pattern in a Slide-Gate Nozzle
(a) Without argon
(b) With argon injection (10% in volume fraction)
(c) Volume fraction (lighter areas have more argon)

Figure 8 shows that five recirculation regions are predicted within the nozzle. Two recirculation zones form in front of and behind the throttling plate, due to the throttling effect of the slide gate. Another is created in the cavity of the slide gate. Finally, the two zones in the upper portion of the ports are associated with the "oversized" nature of the ports of the submerged entry nozzle, relative to its bore. In each of these regions, the flow is recirculating, velocities are relatively low, and a high volume fraction of argon is collected. Very little gas can penetrate to the bottom of the nozzle. This prediction is consistent with water model experiments.

It is important to note that the argon gas expands in volume by a factor of 5~6 when it heats from ambient to the temperature of the molten steel. Heat transfer calculations revealed that argon gas temperature is raised to nearly 99% of the molten steel temperature while in the ceramic nozzle even before it reaches the molten steel. Thus, the gas volume injected for isothermal modeling conditions should be five to six times the flow rate at ambient temperature, if it is intended to match.

These results suggest that argon acts to reduce nozzle clogging in several different ways. Where it is injected into regions of uniform downward flow, such as the lower part of the upper tundish nozzle, a film of argon gas may form (mode IV). Here, the build-up of deoxidization products is prevented by avoiding physical contact between the steel stream and the refractory wall surfaces. However, the gas sheet may lead to "annular flow" [8], where the liquid and gas phases separate in the nozzle. This may be detrimental to flow in the mold because the large gas volumes create disturbances when they leave the nozzle ports intermittantly. Alternatively, argon gas bubbles may mix with the turbulent molten steel, producing a more homogeneous mixture. This occurs in the SEN for the example shown in Fig. 8. Here, flow disturbances at the refractory wall surface, enhanced by argon injection, likely wash away deposits as they form.

4. INCLUSION ATTACHMENT MODEL

A model has been developed to predict the attachment of inclusions to an argon gas bubble rising at constant velocity relative to the surrounding liquid steel. The liquid steel is contaminated by inclusions with a given steady size distribution, based on measurements.

According to this model, an inclusion of radius a_i is attached to a moving bubble if and only if its center follows the streamline that passes above the top point of the bubble's surface within the distance a_i or less. As the bubble travels, it picks up all inclusions of radius a_i that happen to be closer than a critical distance b_i from the axis through the bubble centerline in the direction of flow. The inclusion mass attachment rate [kg/s] is calculated by

$$\dot{m} = U\sum_{i} m_i \pi b_i^2 \qquad (2)$$

Where, U : velocity of the bubble, m_i : mass concentration of inclusions of radius a_i [kg/m^3], b_i :

distance from the bubble centerline in undisturbed flow for the corresponding streamline [m].

4.1 Streamline Calculation

In this model, the streamlines define regions in the undisturbed flow where inclusions of particular sizes are attached. The argon bubble is considered to be a sphere submerged into inviscid (potential) flow of constant local velocity. In this case the classical solution [9] can be used to calculate stream functions using Eq.(3):

$$\psi = \frac{1}{2}Ur^2\sin^2\theta\left(1-\frac{R^3}{r^3}\right) \tag{3}$$

Where, ψ : stream function, U : velocity of the bubble, R : radius of the bubble, $(r,\ \theta)$: spherical polar coordinates with $\theta\ = 0$ in the direction of U.

Streamlines are plotted in Figure 9 by solving Eq (3) for constant ψ, starting from the following boundary condition defined at the top point:

$$\theta = \frac{\pi}{2};\quad r = l_i\ ;\quad l_i = R + a_i \tag{4}$$

where, l_i : distance from the center of the bubble to the streamline at the top point, a_i : distance from the surface of the bubble to the streamline at the top point.

After converting polar coordinates into Cartesian, the distance from the bubble axis to the streamline is calculated by:

$$y(r) = r\sqrt{\frac{l_i^2 - R^3/l_i}{r^2 - R^3/r}}\quad ;\quad x(r) = \sqrt{r^2 - y^2} \tag{5}$$

Centers of inclusions are assumed to follow the streamlines of the flow around the bubble. As illustrated in Figure 9, if the streamline i passes near the top point of the bubble surface within the distance a_i , then any inclusion of radius a_i or larger is attached to the bubble.

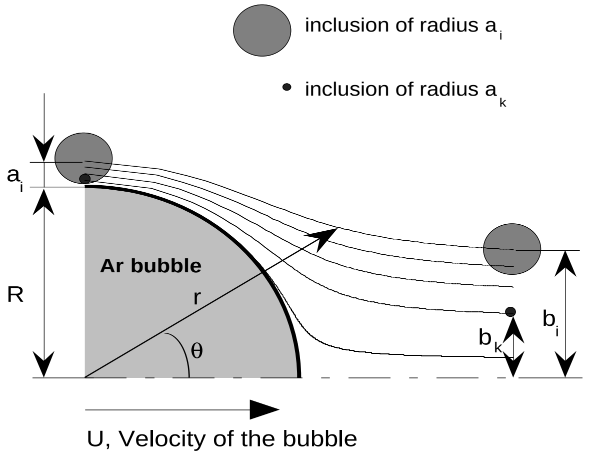

Figure 9 Inclusion attachment to a bubble

For each inclusion of radius a_i, the corresponding distance y = b_i is calculated from the streamlines using Eq. (5) at large x or r. This is the distance between the line passing through the center of the bubble parallel to the bubble's velocity vector and the streamline i in the region of undisturbed flow ahead of the bubble.

The dependence between b_i and a_i is presented in Figure 10 for bubbles of different sizes. Inclusions of larger radii have slightly larger regions of entrapment.

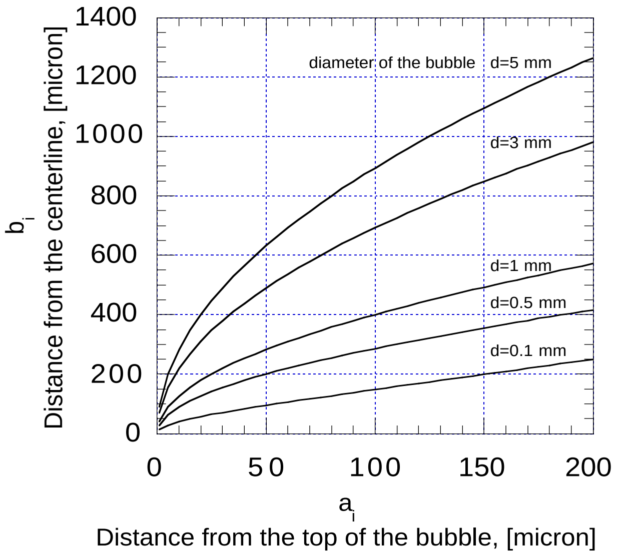

Figure 10 Calculated distance from the bubble axis, b_i, where inclusions will be trapped, as a function of the inclusion radius, a_i, and the bubble diameter.

4.2 Inclusion Distribution

The alumina inclusion mass distribution measured in [10] is used to calculate the mass of inclusions attaching to each bubble as it moves through the steel (Figure 11).

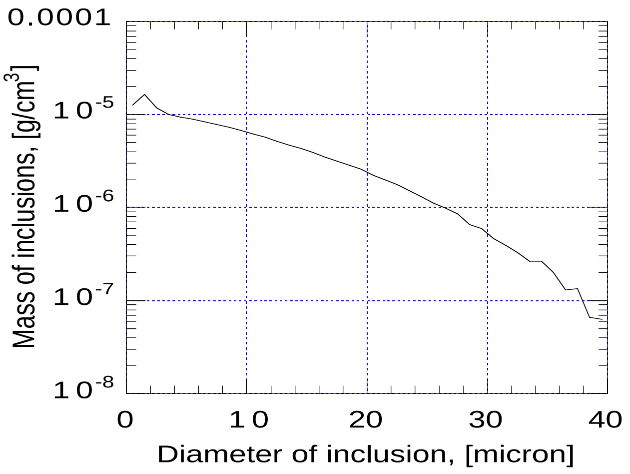

Figure 11 Measured inclusion mass distribution [10]

This inclusion mass distribution corresponds to the weight of alumina for a total oxygen content in the steel of 10.57 ppm and is scaled proportionally for cases with different oxygen content.

It is more convenient to present the results relative to 1 meter travel, rather than to velocity of the bubble. Figure 12 shows the predicted mass of inclusions which attach to an argon gas bubble traveling 1 meter through inclusion distributions with different ppm oxygen, and the same relative distribution as Figure 11.

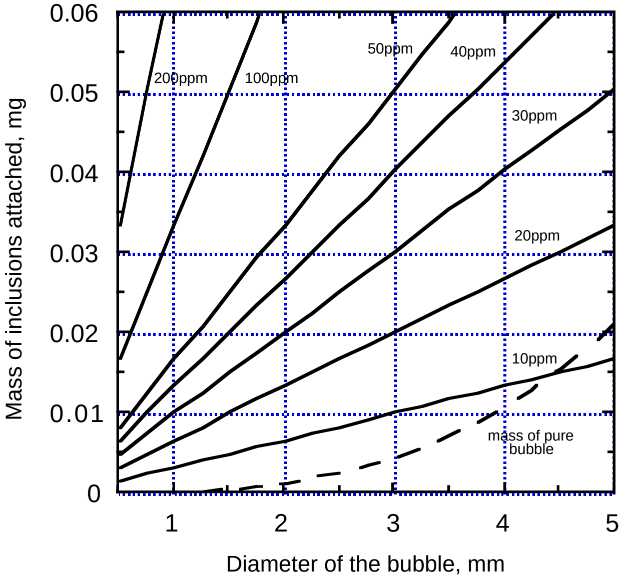

Figure 12 Rate of inclusion mass attachment to moving gas bubbles per meter of bubble travel

These results can be expressed by the following equation for the total mass of inclusions attached to a bubble:

$$M = 3.3 \cdot 10^{-7} D_{bub} O_{ppm} L \tag{6}$$

Where, M : mass of attached alumina inclusions [kg], D_{bub} : diameter of the argon bubble [m], O_{ppm} : weight fraction Oxygen (as inclusions) in steel [ppm], L : distance traveled by the bubble [m].

The mass of attached inclusions increases linearly both with distance travelled and with bubble diameter. Thus, small bubbles are more efficient at removing inclusions per unit volume of gas. Through this mechanism, argon bubbles have a significant influence both in agglomerating the inclusions and then helping to remove them from the mold via flotation.

4.3 Terminal Velocity

A bubble submerged in liquid rises toward the surface with a constant velocity relative to the fluid, called terminal velocity. The terminal velocity V_t is determined by Eq.(7):

$$V_t = \sqrt{\frac{\frac{4}{3} D_{bub} (\rho_s - \rho_a) g}{\rho_s C_d}} \tag{7}$$

Where, C_d : drag coefficient, $\mathrm{Re} = \frac{V_t D_{bub} \rho_s}{\mu_s}$: Reynold's number, V_t : bubble terminal velocity [m/s], D_{bub} : diameter of the bubble [m], ρ_s : density of steel [kg/m^3], ρ_a : density of Argon [kg/m3], g : gravitational acceleration [m/s^2], μ_s : steel viscosity [Ns/m^2], σ : surface tension [N/m].

Small Argon bubbles (up to 0.9mm in diameter) are subject to Stokes law, but when the bubble becomes larger, its shape changes and the drag coefficient is calculated by Tadaki and Maeda model [11] Eq.(8).

$$C_d = \begin{cases} \frac{24}{\mathrm{Re}} & if \quad 0 < \mathrm{Re}\, M^{0.23} \le 8M^{0.068} \\ 0.076\left(\mathrm{Re}\, M^{0.23}\right)^{1.82} & if \quad 8M^{0.068} < \mathrm{Re}\, M^{0.23} \le 6 \\ 1.25\left(\mathrm{Re}\, M^{0.23}\right)^{0.26} & if \quad 6 < \mathrm{Re}\, M^{0.23} < 16.5 \end{cases} \tag{8}$$

where dimensionless parameter, $M = \frac{g \mu_s^{\,4}}{\rho_s \sigma^3}$.

The terminal velocity depends on the drag coefficient which depends on Re number which in turn depends on the terminal velocity. Thus calculations are performed in iterative manner. The following values are used for physical properties of hot expanded argon gas at 1550 ˚C:

ρ_s =7000 kg/m^3 , μ_s =5.6e-3 Ns/m^2 , ρ_a =0.3241 kg/m^3, σ =1.2 N/m.

The terminal velocity of Argon gas bubbles in molten steel is shown in Figure 13:

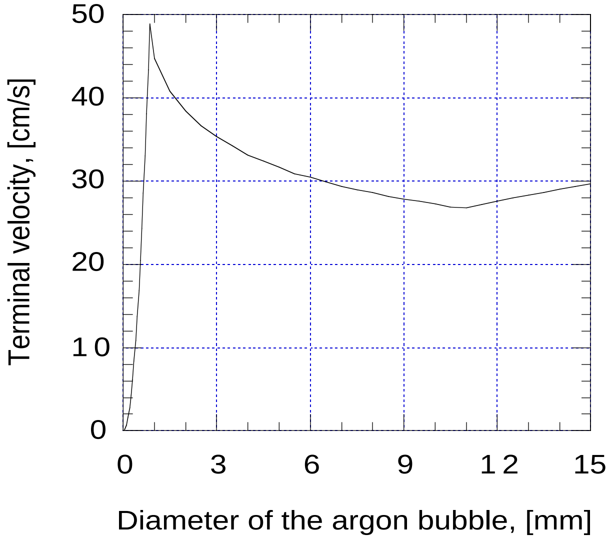

Figure 13 Argon gas bubble terminal velocity

The drag coefficient is calculated using the first rule of Eq.(8) (Stokes law) for bubbles less than 0.9 mm in diameter. The second rule is for bubble diameters between 0.9mm and 11mm and the third rule is for bubbles larger than 11mm.

Bubbles with diameters near 1 mm float the fastest. Further increase in bubble diameter causes terminal velocity to decrease until the bubble's diameter exceeds 11mm.

The attaching inclusions have a negligible effect on the terminal velocity of the bubble. For example, an argon bubble of 0.5 mm in diameter has a terminal velocity of 17.11 cm/s. If the bubble travels 3 meters through molten steel with oxygen content of 20ppm it is predicted to attach alumina inclusion with total mass of 0.0165 mg. Bubble terminal velocity drops to 16.73 cm/s, which is only 2.2% less.

5. ARGON BUBBLE MOVEMENT IN THE MOLD

A 3-D finite-difference model has been developed using FLUENT to study the movement of the steel and argon gas bubbles through the mold of a typical continuous slab caster. Initial single-phase calculations are performed, neglecting the effect of the argon bubbles on the steel flow pattern. Thus, the results only apply to low argon flow rates. Steady flow is calculated using the k-ε turbulence model.

Figure 14 shows the mean velocity field in the middle plane of the mold. The flow field is calculated in a 4-m long liquid domain contained within the solidifying shell. The domain includes the mold and submold, which is curved with a radius of 10m.

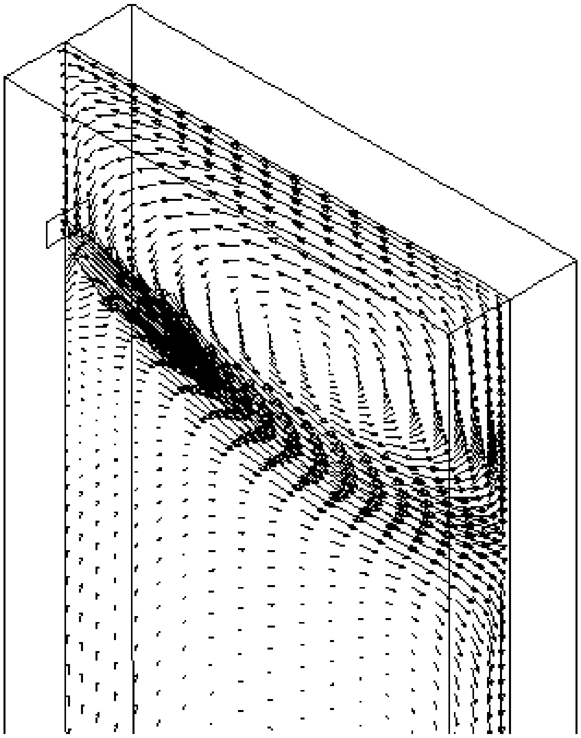

Figure 14 Flow pattern in middle plane of the mold.

Due to symmetry, only one half of the 230 x 1520 mm strand width is modeled. The inlet jet exits at 15° down from a 50 high x 80 mm wide inlet, representing the lower portion of a typical bifurcated nozzle port, with 0° spread angle. The port is submerged 260mm below the meniscus.

Bubble trajectories are calculated through the molten steel using a Lagrangian approach, including the forces of drag and buoyancy. The effects of turbulence are included in some particle traces using the "random walk" feature in FLUENT. This generates a random velocity fluctuation at each step, whose magnitude varies with the local turbulent kinetic energy level. Sample results for bubbles of 0.3mm in diameter are presented in Figure 15. Most of the bubbles "escape" by touching the top surface. One particular bubble is "trapped" by touching the inside radius of the strand near mold exit.

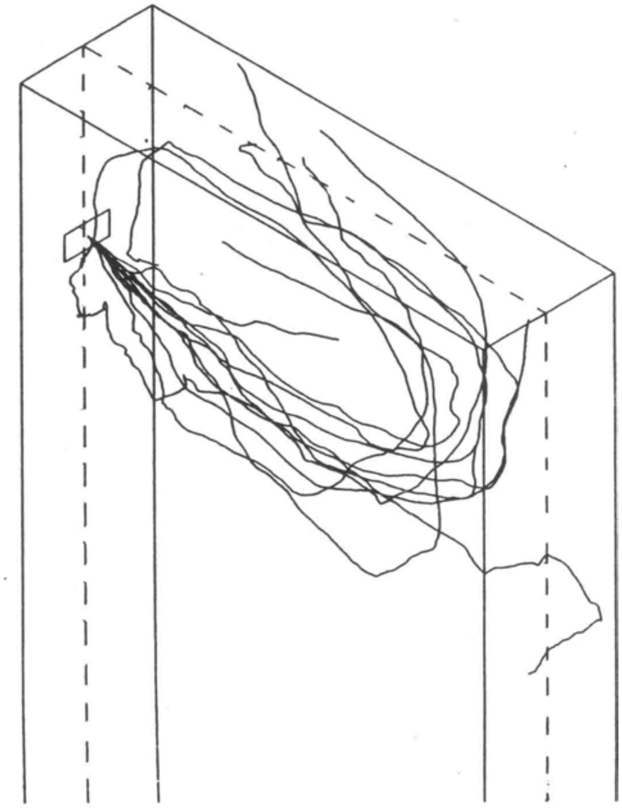

Figure 15 Sample trajectories of 0.3 mm argon bubbles with turbulent motion

The trajectories of several hundred individual particles were calculated, for a casting speed of 1 m/min (40 ipm), including both argon bubbles and alumina inclusions. Table I contains the statistics summarizing these results.

Table I. Particle tracking results

Particle	Case	esc	tra	ex	ab	V_t m/s
Ar bubble d = 0.9mm	M-35	100	0	0	0	0.45
	T-100	62	38	0	0	
	T-490	57	43	0	0	
Ar bubble d = 0.5mm	M-35	94	6	0	0	0.168
	T-100	51	47	2	0	
	T-490	56	44	0	0	
Ar bubble d = 0.3mm	M-35	97	0	0	3	0.06
	T-100	46	44	0	10	
	T-490	36	54	0	10	
Alumina d = 208 micron	M-35	57	23	0	20	0.014
	T-100	24	72	0	4	
	T-490	21	73	0	6	
Alumina d = 30 micron	M-35	0	37	51	12	3e-4
	T-100	16	82	2	0	
	T-490	9	90	1	0	

Abbreviations in Table I mean the following:

M-35 : 35 particles are traced in the mean velocity field. No turbulent effects accounted for. The initial particle locations are distributed across the inlet from the nozzle.

T -100 : 100 particles are traced, taking into account turbulent effects. All particles are injected in the center of the inlet.

T-490 : 490 particles are traced, taking into account turbulent effects. Particles are injected in 14 bunches of 35, distributed across the inlet.

Numbers in the table reflect percentages of particles that:

esc: escaped - floated out to the top surface;
tr : trapped - entrapped in the solidifying shell;
ex : exited - exited computational domain and trapped below 4 m from the meniscus;
ab: aborted - still moving when tracing simulation ended.

Most of the bubbles circulate in the upper mold area and float out to the slag layer. Many inclusions behave similarly, as shown by three of the inclusions in Figure 16. Bubbles circulating in the upper recirculation region without random turbulent motion eventually float out. Bubbles with turbulent motion often touch against the solidification front, as shown by the example trace in Figure 15 and the results in Table I. This occurs on both the inside and outside radius with almost equal frequency, particularly near the narrow faces high in the mold, where the shell is thin (<20mm). It is likely that only some of these bubbles stick, when there is a solidification hook, or other feature on the solidification front to catch them. This entrapment location does not correspond to pencil pipe defects.

A few bubbles manage to penetrate into the lower recirculation zone. Here, a very small argon bubble likely behaves in a similar manner to a large inclusion cluster. Specifically, a 0.15mm bubble has a similar terminal velocity to a 208-micron solid alumina inclusion, whose trajectories are plotted in Figure 16. These particles tend to move in large spirals within the slow lower recirculation zones, while they float towards the inner radius of the slab. At the same time, the bubbles are collecting inclusions. When they eventually touch the solidifying shell in this depth range, entrapment is more likely on the inside radius. This could occur anywhere along their spiral path, which extends from roughly 1-3m below the meniscus. Table I indicates a slight trend that smaller bubbles are more likely to enter the lower zone to be entrapped. However, the event is relatively rare for any bubble size, so the lack of sufficient stastics and random turbulent motion mask this effect.

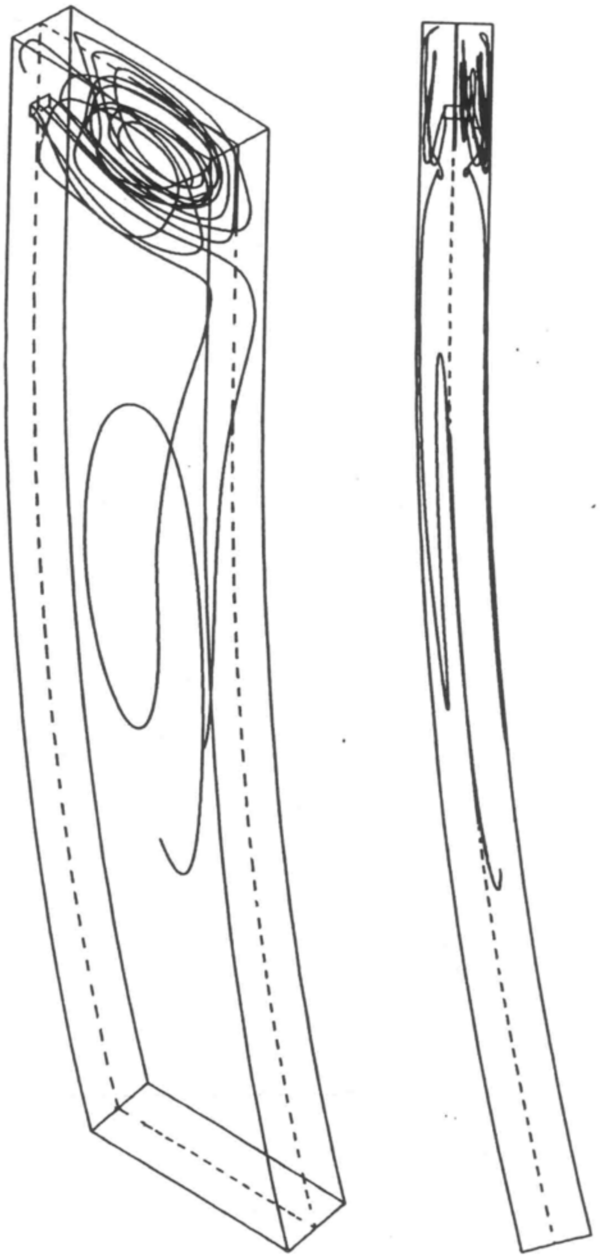

Figure 16 Five sample trajectories of 208-micron solid alumina inclusion particles

Bubbles entrapped in the lower recirculation zone likely lead to defects later during secondary treatment of the slab, especially if they are surrounded by a cluster of inclusions.

6. ARGON BUBBLE ENTRAPMENT IN SHELL

Argon bubbles may be entrapped on the inside radius of the solidifying shell, as illustrated in Figure 16. Although argon bubble entrapment should be similar for all grades cast under the same flow conditions, it leads to severe surface defects in low strength steel, such as ultra-low carbon steel. When the slab is rolled into thin product, the subsurface bubbles elongate. Later during annealing, they can expand to raise the surface of the sheet locally, creating defects such as blisters or "pencil pipe" [12-14]. Hydrogen has been found with the argon in the defects, presumably contributing to higher bubble pressures [15]. The bubbles may be associated with alumina inclusions, or with mold flux inclusions, which may become entrained by high speed flow across the meniscus and foaming [12].

Measurements were made at LTV Steel to determine the depth of rolled argon bubbles beneath the surface of several steel sheets. [13] Assuming that the fractional depth of the bubble across the thickness did not change with rolling, the depth of each bubble beneath the original slab surface was calculated. These are plotted in Figure 17 as a function of casting speed. A distinct trend is apparaent that bubbles are found closer to the surface at higher casting speeds.

Assuming that the bubbles are trapped in the advancing solidification front, their depth should indicate where in the strand they were captured. The relationship between shell thickness and distance beneath the meniscus is illustrated in Figure 18, based on calibrated calculations using a 1-D solidification model [16].

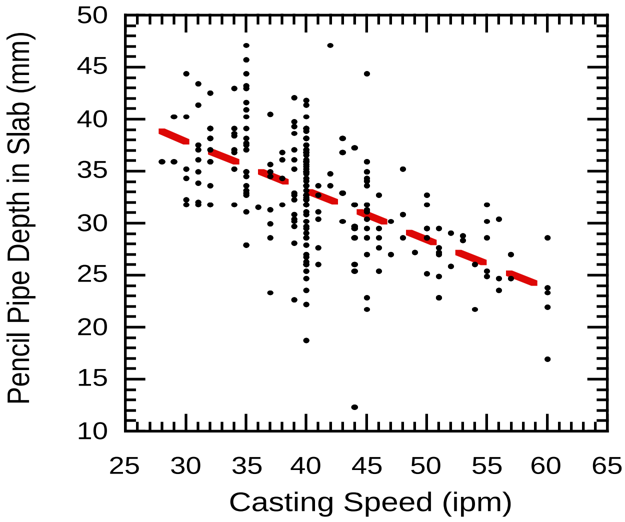

Figure 17 Effect of casting speed on measured depth of argon bubble entrapment below surface of slab

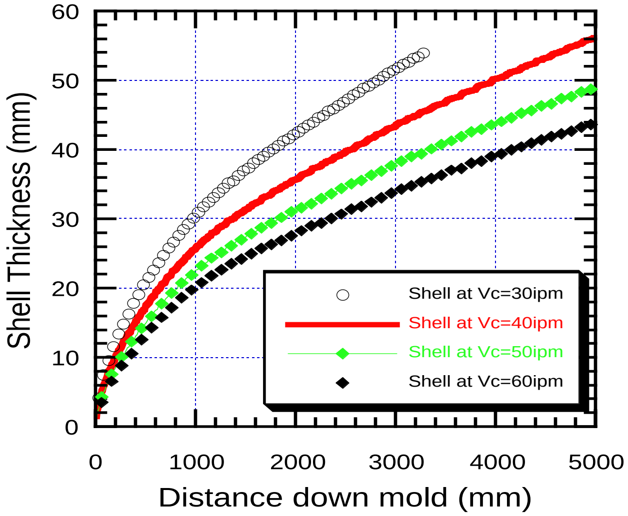

Figure 18 Effect of casting speed on solidified shell growth

Using the shell thickness growth rates in Figure 18, the depth below the meniscus along the strand was calculated for each measured distance below the strand surface. Figure 19 shows the results from Figure 17 transformed in this manner. Now, there is no significant effect of casting speed. Thus, the apparent effect of casting speed on entrapment depth in Figure 17 was due simply to the thinner shell produced at higher speed. The bubbles appear to become entrapped over a charactoristic range of depths averaging 1.8m below the meniscus. This depth roughly corresponds to the region in the lower recirculation zone where bubbles and particles spiral and become entrapped on the inside radius.

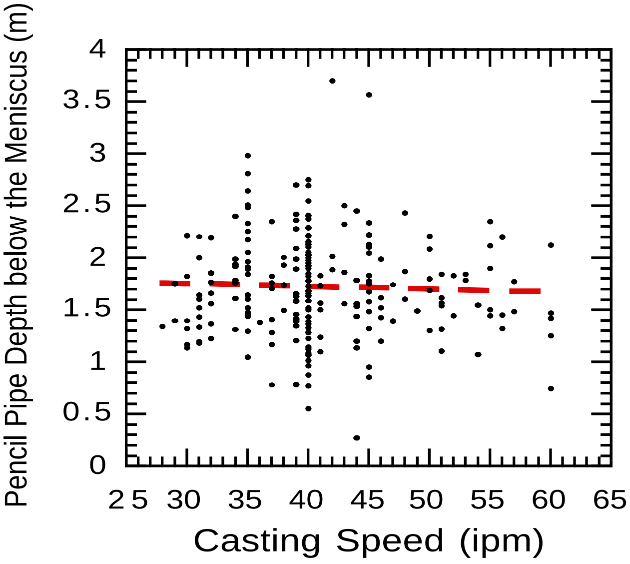

Figure 19 Effect of casting speed on measured depth of argon bubble entrapment below meniscus

It is well-known that pencil-pipe defect incidence increases with casting speed (or flow rate) [12,14]. The finding in this work suggests that the reason is not due to a simple change in flow pattern that has deeper penetration. Rather, this work suggests that the detrimental effect of higher casting speed is likely due to increasing the number of bubbles entering the lower recirculation zone, or making their attachment to the solidification front easier. It is possible that transient effects leading to the intermittant shedding of larger vortexes to lower regions of the mold may contribute to this entrainment of argon bubbles in the lower recirculation zone [17].

7. CONCLUSIONS

This work has combined physical water modeling, mathematical modeling, and plant experimentation to increase understanding of argon bubble behavior during continuous slab casting. Specific findings include:

1) Argon bubble size increases with increasing gas flow rate and decreasing steel flow rate.

2) At high gas flow rates, a gas film may form to help prevent nozzle clogging but create annular flow.

3) The bubbles concentrate within low-velocity regions of the nozzle, which also tend to have flow recirculation. These regions include the slide gate region, and the upper portion of each exit port.

4) Argon bubbles collect inclusions and greatly enhance their removal.

5) Most argon bubbles move through the upper recirculation zone in the mold and exit the top of the mold through the powder layer. A few small bubbles and inclusions enter the lower recirculation zone and spiral towards the inner radius, becoming entrapped in the solidifying shell.

6) Argon bubbles become entrapped at a characteristic distance down the strand which corresponds to the lower recirculation zone and does not depend on the casting speed. These bubbles initiate defects such as pencil pipe during later processing.

ACKNOWLEDGEMENTS

The authors wish to thank researchers at Inland and LTV for providing plant data and the members of the Continuous Casting Consortium at UIUC, which includes Armco Inc. (Middletown, OH), AK Steel, (Middletown, OH), Allegheny Ludlum (Brackenridge, PA), BHP Steel Research (Mulgrave, Australia), Inland Steel (East Chicago, IN), LTV Steel (Cleveland, OH), and Stollberg Inc. (Niagara Falls, NY) for support of this work. Thanks are also due to NCSA at UIUC for computing time and the FLUENT CFD code. Final thanks are extended to J. Mazumder, (Univ. of Michigan) for use of the video camera.

REFERENCES

[1]. Mazumdar, D. and R. Guthrie: *ISIJ International*, Vol.35(1) 1995, pp.1-20.
[2]. Iguchi, M. et. al.: *ISIJ International.*, vol 35(11), pp.1354-1361.
[3]. Davidson, L. and Amick, E.H., Jr.: *AIChE J.,* 1956, vol.2, pp.337-342.
[4]. Datta, R.L. and Napier, D.H.: *Trans. Instn. Chem. Engrs.* (London) 28, 27 (1950).
[5]. Winterton, R.H.S, *Chemical Engineering Science,* 1972, vol.27 pp.1223-1230.
[6]. Irons, G.A. and Guthrie, R.I.T.: *Metall. Trans.,* 9B(1978), pp.101.
[7] Soo, S.L.: Fluid Dynamics of Multiphase Systems, Blaisdell Publishing Company, 1967.
[8] Burty, M. et al: “Experimental and Theoretical Analysis of Gas and metal flows in submerged entry nozzles in Continuous Casting”, PTD Conference Proceedings, ISS, 1995, pp. 287-292.
[9] White, F.M.: ”Viscous Fluid Flow”, McGraw-Hill Inc., p178, 1991.
[10] Miki, Y. et al: personal communication, Kawasaki Steel, 1996.
[11] Tadaki, T. and Maeda, S.: “On the Shape and Velocity of Single Air Bubbles Rising in Various Liquids”, Chemical Engineering (Japan), v25, pp254-264, 1961.
[12] Emling, W. et al: “Subsurface Mold Slag Entrainment in Ultra-low Carbon Steels”, Steelmaking Conference Proceedings, ISS, 1994, pp. 371-379.
[13] Waugaman, T.A. et al: LTV Steel Research, unpublished research, 1995.
[14] Knoepke, J. et al: “Pencil Blister Reductions at Inland Steel Company”, Steelmaking Conference Proceedings, ISS, 1994, pps. 381-388.
[15] Abbel, G. et al: “Argon Bubbles in Slabs”, ISIJ International, Vol. 36, 1996, pp. s219-s222.
[16] Thomas, B.G. et al: “Effect of Transverse Depressions and Oscillation marks on heat transfer in the continuous casting mold”, Sensors and Modeling in Materials Processing”, S. Viswanathan, R. Reddy and J. Malas eds., TMS, 1997, pp. 117-142.
[17] Huang, X. and Thomas, B.G.: “Modeling of Transient Flow Phenomena in Continuous Casting of Steel”, 35th Conf. of Metallurgists, CIM Conference Proceedings, Montreal, Aug. 25-29, 1996, pp. 129-145.